ACS NANO
Cite This: ACS Nano XXXX, XXX, XXX−XXX
www.acsnano.org

ARTICLE

Piezo-phototronic Effect Enhanced Photodetector Based on $CH_3NH_3PbI_3$ Single Crystals

Qingsong Lai,[†,‡,∥] Laipan Zhu,[†,‡,∥] Yaokun Pang,[†,‡] Liang Xu,[†,‡] Jian Chen,[†,‡] Zewei Ren,[†,‡] Jianjun Luo,[†,‡] Longfei Wang,[†,‡] Libo Chen,[†,‡] Kai Han,[†,‡] Pei Lin,[†,‡] Ding Li,[†,‡] Shiquan Lin,[†,‡] Baodong Chen,[†,‡] Caofeng Pan,*[,†,‡,⊥] and Zhong Lin Wang*[,†,‡,§,⊥]

[†]CAS Center for Excellence in Nanoscience, Beijing Key Laboratory of Micro-nano Energy and Sensor, Beijing Institute of Nanoenergy and Nanosystems, Chinese Academy of Sciences, Beijing 100083, P.R. China

[‡]School of Nanoscience and Technology, University of Chinese Academy of Sciences, Beijing 100049, P.R. China

[§]School of Material Science and Engineering, Georgia Institute of Technology, Atlanta, Georgia 30332, United States

[⊥]Center on Nanoenergy Research, School of Physical Science and Technology, Guangxi University, Nanning 530004, P.R. China

Supporting Information

ABSTRACT: **Piezoelectric organic−inorganic lead halide perovskites have recently attracted much attention in the field of optoelectronic devices. However, their piezoelectric properties as a possible way to modulate device performances have rarely been reported. Here, we study experimentally a photodetector based on $CH_3NH_3PbI_3$($MAPbI_3$) single crystals, whose performance is effectively modulated *via* an emerging effect—the piezo-phototronic effect, which is to use the piezoelectric polarization charges to tune the optoelectronic processes at the interface. A piezoelectric coefficient of 10.81 pm/V of the $CH_3NH_3PbI_3$ single crystal is obtained. Under 680 nm laser illumination with a power density of 3.641 mW/cm^2 and at an external bias of 2 V, compared to the case without straining, the light current of the photodetector is enhanced by ∼120% when a 43.48 kPa compressive pressure is applied. The response speed of the photocurrent is 3 and 2 times faster than the cases without applying pressure for the light-on and light-off states, respectively. This work proves that the performance of the photodetector based on $MAPbI_3$ single crystals can be effectively enhanced by the piezo-phototronic effect, providing a good method for optimizing the performance of future perovskite-based optoelectronic devices.**

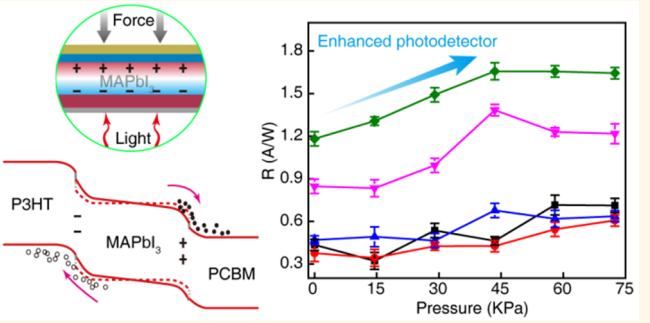

KEYWORDS: *piezopotential, piezoelectric charges, piezo-phototronic effect, perovskite-based single crystal, photodetectors*

In the past few years, we have witnessed the explosion of research on optoelectronic devices based on hybrid organic−inorganic perovskites. The excellent charge carrier transport in organolead halide perovskites is one major contributor to the high performance of these perovskite-based devices.[1−4] Among these devices, solution-processed broadband perovskite-based photodetectors have attracted significant interests, owing to their appropriate direct band gap,[5] large absorption coefficient,[6] long charge carrier lifetime and diffusion length,[7−9] high electrical mobility,[10] and so on. There are many ways to enhance the performance of the perovskite-based photodetectors, such as p−n junction interface engineering, perovskite layer morphology improvement, electrode optimization, *etc.*[11−13] Recently, the piezo-phototronic effect was extensively utilized to enhance the performance of optoelectronic devices such as photodetectors,[14−16] solar cells,[17,18] and light-emitting diodes.[19,20] Upon normal stress, owing to the noncentrosymmetric crystal structure, the piezoelectric polarization charges and piezopotential in the micro/nanostructures at the heterojunction or interface can effectively modulate the band structure of the heterojunction and tune the charge separation, transport, and/or recombination in optoelectronic processes, which is the basic principle of the piezo-phototronic effect.[21−23]

It would be desirable if the emerging piezo-phototronic effect can work effectively on promising perovskite-based

Received: August 16, 2018
Accepted: October 2, 2018
Published: October 2, 2018

DOI: 10.1021/acsnano.8b06243
ACS Nano XXXX, XXX, XXX−XXX

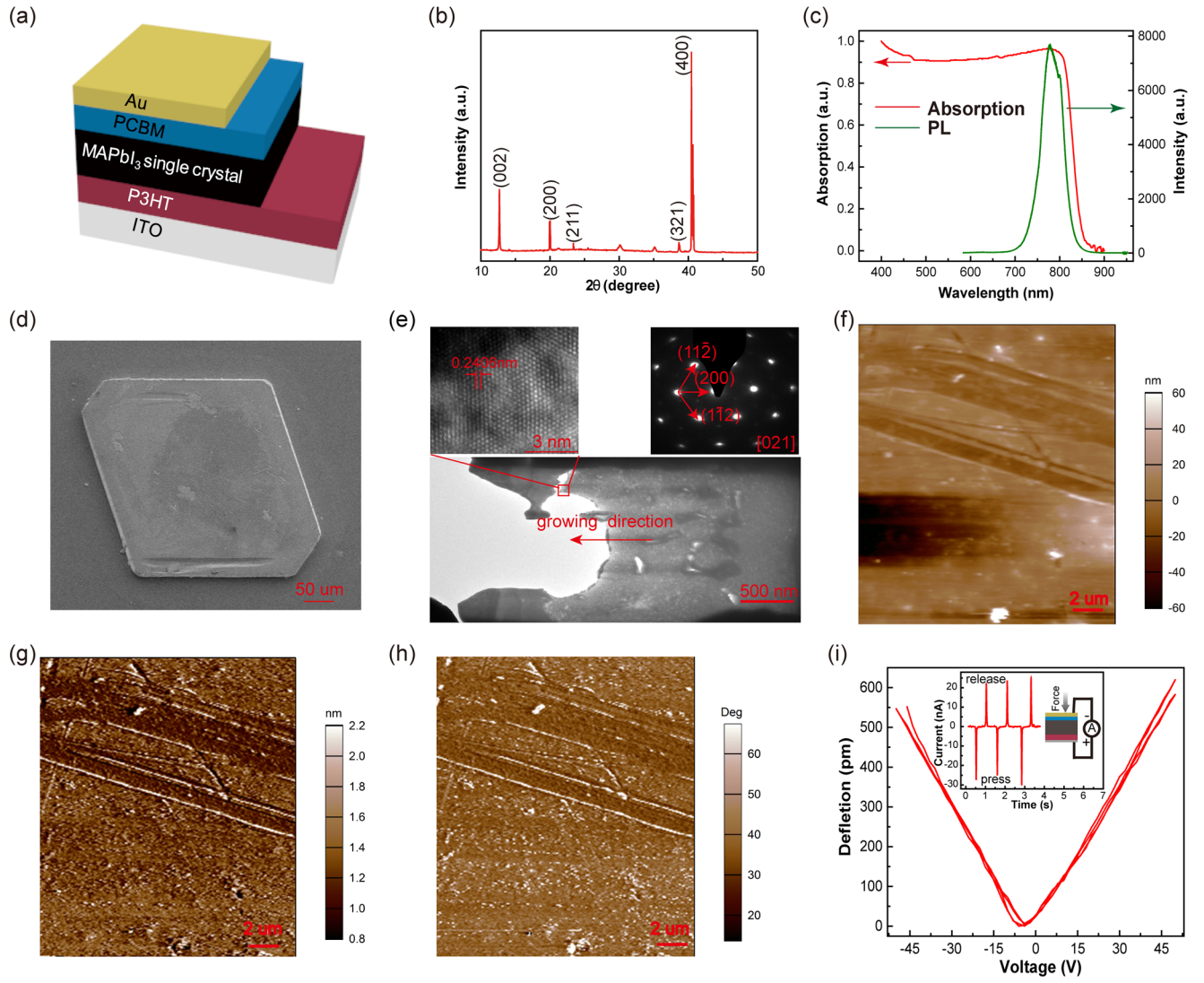

Figure 1. Characterization of the device. (a) Device structure of the photodetector based on the $MAPbI_3$ single crystal. (b) XRD of the $MAPbI_3$ single crystal. (c) PL and absorption spectra of the $MAPbI_3$ single crystal. (d) SEM image of the $MAPbI_3$ single crystal. (e) TEM image of the $MAPbI_3$ single crystal, indicating that the growth plane of the $MAPbI_3$ single crystal is along (200), where the top left inset is the HR-TEM image, the top right inset is the SAED pattern, and the bottom one is a cross-sectional SEM graph of the sample after the process of FIB technology. (f) Topography, (g) amplitude, (h) phase two-dimension images of the $MAPbI_3$ single crystal obtained from PFM measurement, whose bias is set to be 20 V. (i) Deflection−voltage characteristics show good piezoelectric performance of the $MAPbI_3$ single crystal. The inset is a piezoelectric nanogenerator, indicating negative and positive current when pressing and releasing a force, respectively.

photodetectors. Using the piezoelectric properties, the hybrid perovskites have shown potential applications as piezoelectric nanogenerators or energy-harvesting devices.[24,25] For $CH_3NH_3PbI_3$ single crystals, a d_{33} value of 2.7 pm/V was reported from direct optical measurement.[26] A local d_{33} value of 6 pm/V was obtained *via* piezoresponse force microscopy (PFM) in $MAPbI_3$ polycrystalline thin films, whereas the average piezoresponse of the films over a large scale can be reduced sharply to a negligible level due to the disordered molecular dipoles.[27,28] Therefore, $MAPbI_3$ single crystals with a relatively large piezoelectric coefficient might be good candidates in the study of piezo-phototronic effect enhanced perovskite-based photodetectors. In addition, perovskite single crystals are shown to have much longer carrier diffusion length well above tens of micrometers due to the absence of grain boundaries and significantly reduced defect density.[26,29,30]

In this work, a photodetector based on $MAPbI_3$ single crystals is prepared, and its performance enhancement by piezo-phototronic effect is investigated as a function of light power density and vertical pressure. A piezoelectric coefficient of 10.81 pm/V of the $MAPbI_3$ single crystals is obtained *via* PFM measurement. At a power density of 3.641 mW/cm^2 for a 680 nm laser, the photocurrent can be improved by ~120% *via* the piezo-phototronic effect under a pressure of 43.48 kPa. The response speed of the photocurrent is 3 and 2 times faster compared to the case without pressure for the light-on and light-off states, respectively. It is believed that this enhancement is due to the modulated energy bands *via* piezoelectric polarization charges produced by external pressure. Although the overall performances of the used photodetectors are not as good as those based on thin-film perovskites, this work provides a fundamentally good way of utilizing the piezo-

DOI: 10.1021/acsnano.8b06243
ACS Nano XXXX, XXX, XXX−XXX

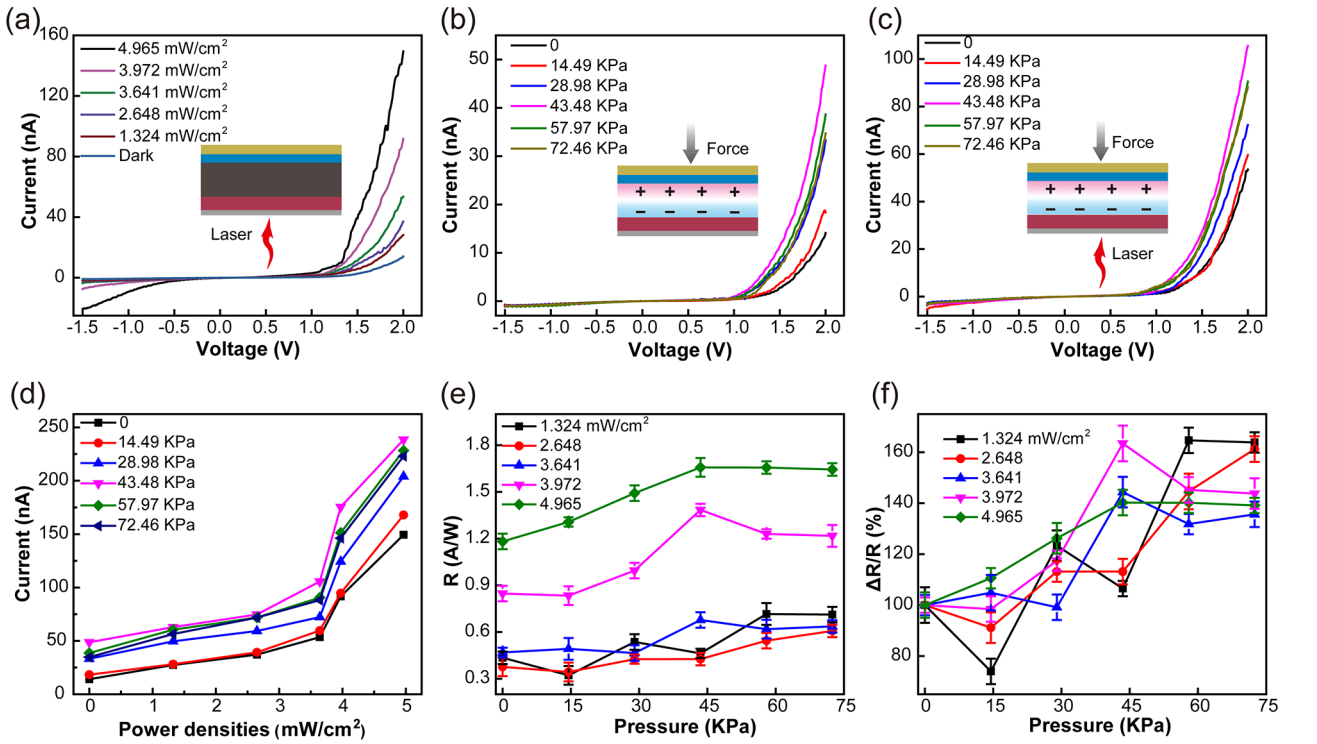

Figure 2. Electrical characteristics of the photodetector and its performance modulation by the piezo-phototronic effect. (a) *I*–*V* characteristics of the device under different power densities. (b) *I*–*V* characteristics of the device under different pressures. (c) *I*–*V* characteristics of the device under different pressures at the power density of 3.641 mW/cm². (d) Relationship between the photocurrent and power density under different pressures at 2 V forward bias. (e) Photoresponsivity and (f) relative change of photoresponsivity of the device under different pressures and different power densities at 2 V forward bias.

phototronic effect to efficiently improve the performance of optoelectronic devices based on perovskite structures.

RESULTS AND DISCUSSION

The structure of the $MAPbI_3$ single-crystal photodetector is schematically illustrated in Figure 1a. First, a thin hole transport layer of poly-3-hexylthiophene (P3HT) is spin-coated on a clean indium-tin oxide (ITO) glass. Then, the $MAPbI_3$ single crystal is grown on the P3HT through a space-confined method,[31] followed by spin-coating a layer [6,6]-phenyl-C61-butyric acid methylester (PCBM) on the $MAPbI_3$ single crystal as an electron transport layer. Then, a gold (Au) layer is deposited on the PCBM layer as the top electrode to form the ITO/P3HT/$MAPbI_3$/PCBM/Au vertical photodetector structure. Finally, the photodetector is enveloped by polydimethylsiloxane (PDMS) to enhance its mechanical endurance. The detailed fabrication processes and measurement setups are shown in the Experimental Section. The X-ray diffraction (XRD) graph reveals a (200) peak, which will be proven to be the growth plane of $MAPbI_3$ single crystals (Figure 1b). Figure 1c displays the steady-state photoluminescence (PL) and absorption spectra of the $MAPbI_3$ single crystal (a compared absorption spectrum of P3HT is shown in Figure S2 (Supporting Information)). The absorption edge of the $MAPbI_3$ single crystal appears at ~840 nm. The PL peak is located between 650 and 850 nm, which is a bit wider toward low wavelength than that in a previous report.[32] Scanning electron microscopy (SEM) image shows a good surface morphology of the $MAPbI_3$ single crystals with four long (~275 μm) and two short (~85 μm) sides, and the thickness is ~50 μm (Figure 1d and Figure S1 (Supporting Information)). High-resolution transmission electron microscopy (HR-TEM) and the corresponding select area electron diffraction (SAED) pattern illustrate that the as-fabricated $MAPbI_3$ possesses a good single-crystal tetragonal structure and that the vertical growth plane is along (200), as shown in the top two graphs of Figure 1e. Here, the $MAPbI_3$ single crystal at room temperature belongs to the *I*4/*mcm* space group.[33,34] A cross-sectional HR-TEM sample is fabricated by focused ion beam (FIB) etching, and the SEM image in Figure 1e denotes the cross-sectional morphology of the etched sample.

The PFM is usually used to characterize the electromechanical response of piezoelectric materials. In this article, a dual AC resonance tracking piezoelectric force microscopy (DRAT-PFM) is utilized to characterize the piezoelectric properties of the $MAPbI_3$ single crystal. Figure 1f shows the contact-mode topography of the $MAPbI_3$ single crystal. The corresponding two-dimensional PFM amplitude and phase images are displayed in Figure 1g,h, respectively, which reveals an obvious piezoelectric behavior on the measured surface of the $MAPbI_3$ single crystal. A piezoelectric coefficient d_{33} is also measured by observing the butterfly curve. Piezoelectric coefficient d_{33} represents the capacity of materials for how many charges can be induced by the deflection caused by compressive pressure. The piezoelectric effect is a reversible process exhibiting both the direct piezoelectric effect (electrical charges generated by an applied mechanical force) and reverse piezoelectric effect (mechanical strain response to an applied voltage). By using the reverse piezoelectric effect, the deflection–voltage characteristics of the $MAPbI_3$ single crystal are obtained, as shown in Figure 1i, from which the

DOI: 10.1021/acsnano.8b06243
ACS Nano XXXX, XXX, XXX–XXX

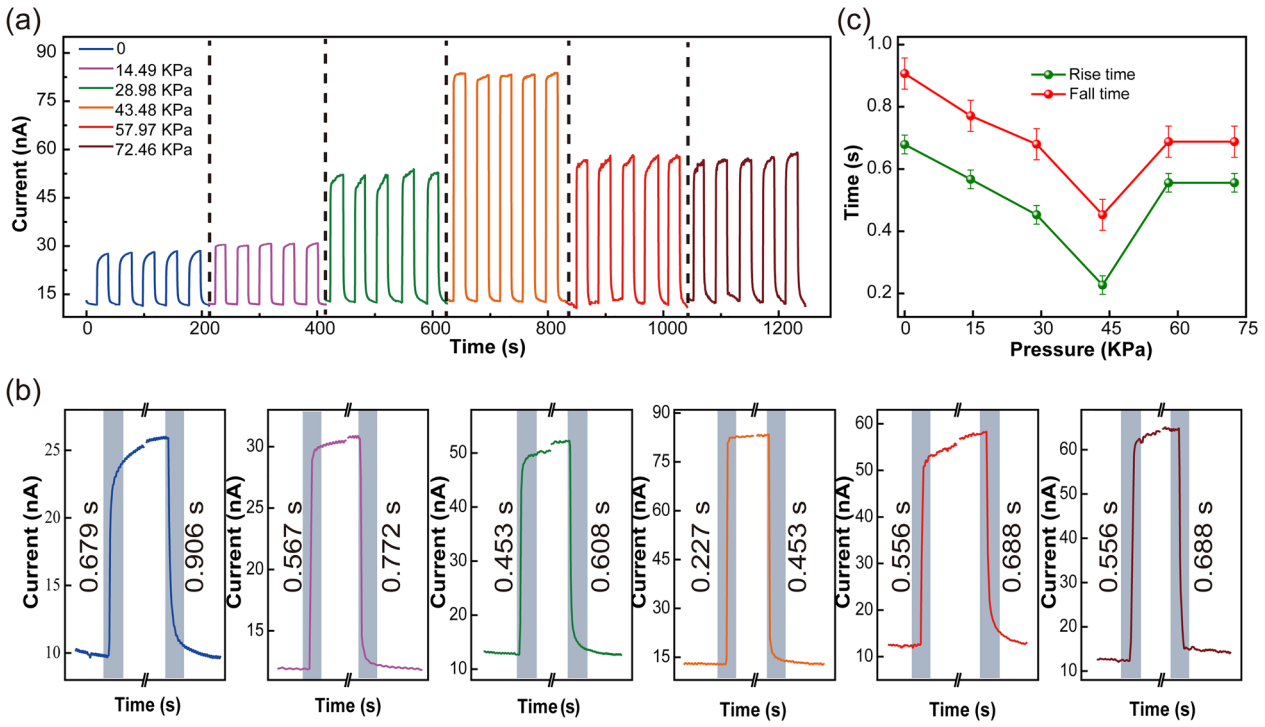

Figure 3. Transient response of the photodetector under different compressive pressures. (a) $I-t$ characteristics of the device under different pressures at 1.5 V forward bias and 2.648 mW/cm^2 power density. (b) Enlarged time response and recovery curves of one cycle for different pressures. (c) Change of rise and fall time under different pressures at the power density of 2.648 mW/cm^2.

piezoelectric coefficient d_{33} in the [100] orientation is calculated to be 10.81 pm/V, which is a bit larger than that measured from local perovskite polycrystal thin films.[27] A ferroelectric effect has been observed in [001] tetragonal-structured lead halide perovskite single crystals.[25,35] However, no ferroelectric effect is found in this $MAPbI_3$ single crystal, which remains unclear.

Unlike the perovskite oxide ferroelectrics (ABO_3 structure), where the piezoelectric property is directly associated with the displacement of ions at different lattice sites, for example, the B-site cations and the oxygens at the tetragonal face center positions, the polarization in these [100]-oriented $MAPbI_3$ single crystals originates from the CH_3NH_3 molecules.[27] If we can find a growth method of $MAPbI_3$ single crystals with a [001] orientation as a preferential direction in the future, the use of [001]-oriented $MAPbI_3$ single crystals might be more desirable because the displacement of ions and realignment of CH_3NH_3 molecules are both existent in this direction. In order to judge the detailed polarization direction under compressive stress, we carry out a piezoelectric nanogenerator measurement by striking the device gently (see the inset of Figure 1i).[26] At the moment of compression, negative current pulses are generated along with piezoelectric potential induced by the piezoelectric charges on the two sides of the $MAPbI_3$ single crystal. As a result, the free electrons in the external circuit move from the ITO to the Au electrode thanks to the piezoelectric potential until it is balanced by the accumulated electrons. When the pressure is released, the induced piezoelectric potential in the $MAPbI_3$ rapidly vanishes and the accumulated electrons near the Au electrode flow back to the bottom electrode, generating positive current pulses. From the reversed direction of current pulses (see the inset of Figure 1i), we can infer that a compressive strain induces charge polarization with negative charges on the bottom and positive charges on the top of the $MAPbI_3$ single crystal.

Next, the electrical characteristics of the $MAPbI_3$ photodetector and its performance modulation by the piezo-phototronic effect under 680 nm illumination are studied in detail, as shown in Figures 2 and 3 and Figures S3 and S4 (Supporting Information). Figure 2a shows the $I-V$ characteristics of the device under different power densities. The photocurrent under 2 V bias increases from 14.11 to 149.41 nA with the power densities increasing from 0 to 4.965 mW/cm^2. When a compressive pressure is applied to the device (that is, to the PDMS) and reaches gradually to 43.48 kPa, the dark current increases from 14.11 to 48.75 nA (Figure 2b). The dark current begins to decrease from 48.75 to 34.73 nA with the compressive pressure further increasing to 72.46 kPa. Then the $I-V$ characteristics of the device under both pressure and light illumination is studied (see Figure 2c). Similar to the case of the dark current, the light-induced photocurrent under the power density of 3.641 mW/cm^2 first increases and then decreases with the increase of compressive pressure. When the compressive pressure increases to 43.48 kPa, the photocurrent under 2 V bias rises from 53.5 to 105.59 nA. When the compressive pressure further increases from 43.48 to 72.46 kPa, however, the photocurrent falls back to 88.16 nA. The photocurrent under 2 V forward bias as a function of power density under different compressive pressures is shown in Figure 2d. It can be found that the photocurrent at 2 V forward bias monotonously increases with the increase of power density under each applied compressive pressure, and the photocurrent at 2 V bias increases with the compressive pressure increasing to 43.48 kPa. Next, the current decreases with the compressive pressure further increasing under each power density. To better understand the photosensing performance of the photodetector, the photoresponsivity R

DOI: 10.1021/acsnano.8b06243
ACS Nano XXXX, XXX, XXX−XXX

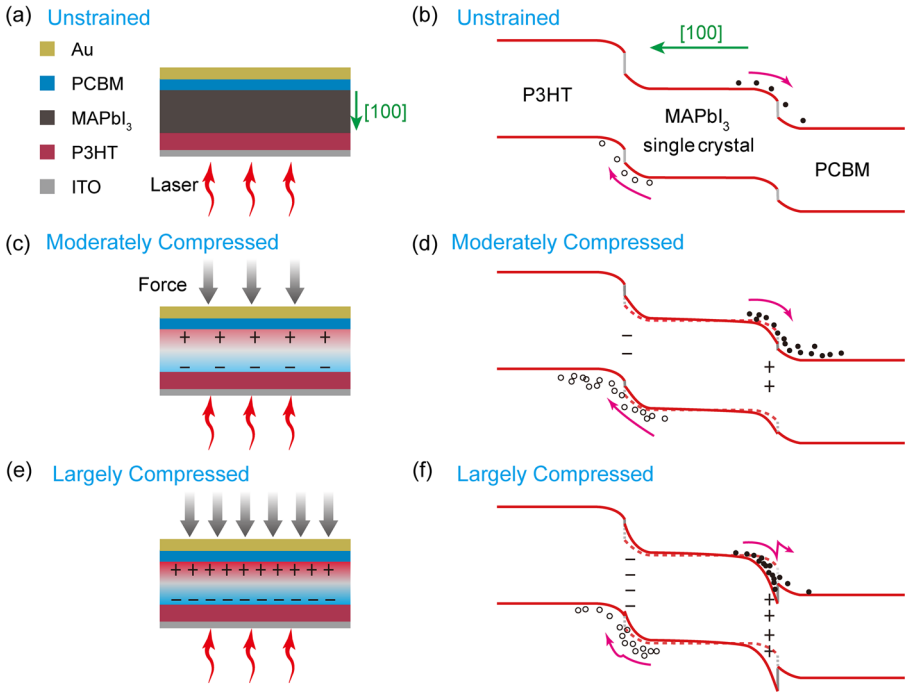

Figure 4. Schematic structure and energy band diagrams of the device. (a) Schematic cross section and (b) energy band diagram of the device without applying pressure. (c) Schematic cross section and (d) energy band diagram of the device under a moderate pressure. (e) Schematic cross section and (f) energy band diagram of the device under a large pressure.

and its relative change $\Delta R/R$ (see Figure 2e,f) are calculated by using expressions:

$$R = \frac{I_{light} - I_{dark}}{P_{ill}} = \frac{\eta_{ext} q}{h\nu} \times \gamma_G$$

and

$$\frac{\Delta R}{R} = \frac{R - R_0}{R_0}$$

where $P_{ill} = I_{ill} \times S$ is the illumination power on photodetector, I_{ill} is the excitation power density, S is the effective area of the photodetector, I_{light} is the photocurrent under illumination, I_{dark} is the dark current, γ_G is the internal gain, η_{ext} is the external quantum efficiency (EQE), q is electronic charge, h is Planck's constant, and ν is the frequency of the light. Under lower power density (<3.641 mW/cm^2), R increases monotonously with increasing pressure. If the power density surpasses 3.641 mW/cm^2, however, the R increases first with the increase of compressive pressure but then decreases as the pressure is enhanced over 43.48 kPa. Under lower power density (<3.641 mW/cm^2), $\Delta R/R$ increases on the whole. When the compressive pressure reaches up to 43.48 kPa and the power density surpasses 3.641 mW/cm^2, $\Delta R/R$ also reaches up to maximum values. The optimal compressive pressure to enhance the performance of the photodetector is around 43.48 kPa. It should be noted that the single crystal shows some pinpoint in the surface of the single crystal, and the $MAPbI_3$ single crystal is thick up to 50 μm, which constrains the transport of carriers in the $MAPbI_3$ single crystal. These make the device photocurrent for this single crystal lower than that for those thin films (usually several micrometers in thickness).

The transient response of the photodetector based on the $MAPbI_3$ single crystal to 680 nm illumination is measured. Figure 3 shows the transient response to the illumination at the power density of 2.648 mW/cm^2 and bias of 1.5 V under different compressive pressures. The transient response under conditions of 3.641 mW/cm^2, 1.5 V; 2.648 mW/cm^2, 2.0 V; and 3.641 mW/cm^2, 2.0 V are shown in Figures S5–S7 (Supporting Information), respectively. From those figures, it can be discovered that the photocurrent increases with the increasing pressure until the pressure is up to 43.48 kPa, and then the photocurrent drops off if the pressure is further increased. The response time shows a similar changing tendency with the compressive pressure. Under the condition of 2.648 mW/cm^2 and 1.5 V, when the compressive pressure is increased from 0 to 43.48 kPa (Figure 3c), the rise time decreases from 0.679 to 0.227 s and the fall time decreases from 0.906 to 0.453 s, which indicates that the response speed has 3- and 2-fold enhancement, respectively. With the compressive pressure further increasing from 43.48 to 72.46 kPa (Figure 3c), however, the rise time increases from 0.227 to 0.556 s and the fall time increases from 0.453 to 0.688 s.

To determine the mechanism of the performance of the photodetector that is improved by the piezo-phototronic effect, the energy band diagrams of the photodetector under different kinds of compressive pressures are carefully analyzed. The band gap of the $MAPbI_3$ single crystal is 1.5 eV (E_V is about −5.4 eV, and E_C is about −3.9 eV). The highest occupied molecular orbital (HOMO) and lowest unoccupied molecular orbital (LUMO) of PCBM are −6.0 and −4.0 eV, respectively. The HOMO and LUMO of P3HT are −5.2 and −3.2 eV, respectively. The schematic energy band diagrams of the photodetector are shown in Figure 4. Figure 4a,b shows the schematic cross section and energy band diagrams of the photodetector under a pressure-free condition, respectively. When the 680 nm laser is directed on the surface of the $MAPbI_3$ single crystal, the photoinduced carriers will be generated. The electron–hole pairs are separated with the help

DOI: 10.1021/acsnano.8b06243
ACS Nano XXXX, XXX, XXX–XXX

of the inner electric field. With the increase of illumination power density, many more photoinduced carriers are generated and separated, so that the photocurrent increases with the increasing power density. When the compressive pressure is applied to the photodetector, piezoelectric polarization charges are generated on the surface of the $MAPbI_3$ single crystal for its noncentrosymmetric structure, and there is piezo-potential simultaneously. From the PFM measurement discussed in Figure 1g–i, [100] directions have a strong piezoelectric effect with a piezoelectric coefficient of 10.81 pm/V. From the piezoelectric nanogenerator measurement (the inset of Figure 1i), we can see that instantaneous press and release induces negative and positive current pulses, respectively. Therefore, under a compressive pressure, the positive and negative piezoelectric charges are produced on the surface of $MAPbI_3$ near PCBM and P3HT, respectively (see Figure 4). Hence the right-side energy band of the $MAPbI_3$ single crystal is moved down, while the left-side energy band is shifted up under a medium compressive pressure, which can enhance the inner electric field and therefore benefit the separation of photogenerated carriers and the reduction of carrier recombination (Figure 4c,d). Therefore, the photocurrent increases under appropriate compressive pressure. The energy difference between the conduction band of the $MAPbI_3$ single crystal and the HOMO of PCBM is small (~0.1 eV). If the compressive pressure is further increased, the piezo-potential becomes larger in the $MAPbI_3$ single crystal, with much more piezoelectric charges generated (Figure 4e). Hence the right-side energy band of the $MAPbI_3$ single crystal is further moved down, which makes the bottom of the conduction band of the $MAPbI_3$ single crystal lower than the HOMO of PCBM. Hence, a potential well is induced that can trap the photogenerated electrons (Figure 4f). As a result, the photocurrent and response speed have a slight decline when the compressive pressure further increases. From the details given above, we can see that this turning point is due to the different value between the bottom of the conduction band of the $MAPbI_3$ single crystal and the LUMO of the PCBM, as well as the piezo-potential in the $MAPbI_3$ single crystal. The piezo-potential is closely related to the Young's modulus, the piezoelectric coefficient, and the thickness of $MAPbI_3$ single-crystal layer, *etc*. However, R and $\Delta R/R$ almost increase all the time with the increase of pressure for lower power densities, which might be due to the improved metal–semiconductor contacts that contribute much more than the trapping effect due to the overlapping energy bands.

CONCLUSIONS

In summary, we fabricated a photodetector based on the $MAPbI_3$ single crystal. The photodetector shows a lower dark current for about 14 nA. Under 680 nm illumination, its photocurrent increases with increasing power density. A piezoelectric coefficient of 10.81 pm/V of the $MAPbI_3$ single crystal is obtained *via* PFM measurement. Under a 3.641 mW/cm^2 illumination and compressive pressure of 43.48 kPa, the photocurrent increases from 53.5 to 105.59 nA, exhibiting an obvious improvement by 120%. The response speed of the photocurrent is 3 and 2 times larger compared to the case without pressure for the light-on and light-off states, respectively. The enhanced photocurrent and response speed are derived from the piezo-phototronic effect. It is worth noting that there is still ample opportunity to enhance the performance of the photodetector by optimizing the device structure, such as reducing the thickness of single crystals, replacing the transport layers with optimal materials, *etc*. This work indicates that the emerging piezo-phototronic effect is demonstrated to be an effective way to enhance the performance of perovskite-based optoelectronic devices.

EXPERIMENTAL SECTION

Device Fabrication. The $MAPbI_3$ single crystal with four long (~275 μm) and two short (~85 μm) sides and a thickness of 50 μm was grown by a hydrophobic interface-confined lateral crystal growth method.[31] ITO glass was cleaned in turn by acetone, alcohol, and deionized water. Then a layer of P3HT film was grown by spin-coating 0.3 wt % P3HT solution in chlorobenzene on the ITO glass at 2000 rpm for 40 s. Then the as-prepared P3HT film was annealed at 100 °C for 10 min. The $MAPbI_3$ precursor with a density of 1.2 M was prepared, which contained PbI_2 and CH_3NH_3I that were dissolved in γ-butyrolactone at 60 °C. The $MAPbI_3$ precursor was dropped onto the glass/ITO/P3HT with another inverted glass/ITO/P3HT covered on it. The reaction occurred at 100 °C for 3 h, and then the reaction temperature was increased to 180 °C and maintained for 3 h; finally, the system was cooled naturally to room temperature. PCBM solution of 1.5 wt % in chlorobenzene was dipped on the top of the thin single crystal with a superfine tip and then annealed at 60 °C for 10 min. After that, a layer of Au was deposited on the top of PCBM as the top electrode by DC magnetron sputtering at room temperature (Denton Discovery 635). Then the photodetector was enveloped by PDMS (~6 cm^2).

Characterization and Measurement. The XRD pattern was acquired with an X'Pert^3 powder X-ray diffractometer. The absorption spectra were recorded by using a UV–vis–NIR spectrophotometer (Shimadzu UV3600). The PL spectrum was obtained by using a confocal microprobe Raman spectroscope (HORIBA/LabRAM HR Evolution). The detailed microscopic structural and morphological characterizations were taken from a HITACHI SU8020 field-emission scanning electron microscope (FE-SEM) and a FEI Tecnai F20 high-resolution transmission electron microscope. The transmission electron microscope sample was fabricated by using dual-beam microscopy combining an advanced focused ion beam with a monochromated FE-SEM (FEI/Helios NanoLab 600i). The AFM image, PFM images, and deflection–voltage characterization were obtained from an Asylum Research/MFP-3D atom force microscope. The electrical characteristics of the devices were recorded with a Keithley 4200-SCS semiconductor parameter analyzer. The output current as a piezoelectric nanogenerator was measured by a Stanford Research Systems Keithley 6514. A MRL-III-680R-100 mW 680 nm laser (Changchun New Industries Optoelectronics Technology Co., Ltd.) with the spot size of 0.5 cm in diameter served as the illumination source. A digital push and pull tester (HP-300) was applied to provide vertical pressures.

ASSOCIATED CONTENT

Supporting Information

The Supporting Information is available free of charge on the ACS Publications website at DOI: 10.1021/acsnano.8b06243.

Additional information and figures (PDF)

AUTHOR INFORMATION

Corresponding Authors

*E-mail: cfpan@binn.cas.cn.

*E-mail: zhong.wang@mse.gatech.edu.

ORCID

Caofeng Pan: 0000-0001-6327-9692

Zhong Lin Wang: 0000-0002-5530-0380

Author Contributions

‖Q.L. and L.Z. contributed equally to this work.

DOI: 10.1021/acsnano.8b06243
ACS Nano XXXX, XXX, XXX–XXX

Notes

The authors declare no competing financial interest.

ACKNOWLEDGMENTS

This research was supported by the National Key R&D Project from Minister of Science and Technology (2016YFA0202704), Beijing Municipal Science & Technology Commission (Z171100000317001, Z171100002017017, Y3993113DF), and National Natural Science Foundation of China (Grant Nos. 11704032, 51432005, 5151101243, 51561145021).

REFERENCES

(1) Calió, L.; Kazim, S.; Grätzel, M.; Ahmad, S. Hole-Transport Materials for Perovskite Solar Cells. *Angew. Chem. Int. Ed.* **2016**, *55*, 14522−14545.

(2) Zhu, H.; Fu, Y.; Meng, F.; Wu, X.; Gong, Z.; Ding, Q.; Gustafsson, M. V.; Trinh, M. T.; Jin, S.; Zhu, X. Y. Lead Halide Perovskite Nanowire Lasers with Low Lasing Thresholds and High Quality Factors. *Nat. Mater.* **2015**, *14*, 636.

(3) Wang, Z.; Yu, R.; Pan, C.; Li, Z.; Yang, J.; Yi, F.; Wang, Z. L. Light-Induced Pyroelectric Effect as an Effective Approach for Ultrafast Ultraviolet Nanosensing. *Nat. Commun.* **2015**, *6*, 8401.

(4) Tan, Z.-K.; Moghaddam, R. S.; Lai, M. L.; Docampo, P.; Higler, R.; Deschler, F.; Price, M.; Sadhanala, A.; Pazos, L. M.; Credgington, D.; Hanusch, F.; Bein, T.; Snaith, H. J.; Friend, R. H. Bright Light-Emitting Diodes Based on Organometal Halide Perovskite. *Nat. Nanotechnol.* **2014**, *9*, 687.

(5) Jeng, J.-Y.; Chiang, Y.-F.; Lee, M.-H.; Peng, S.-R.; Guo, T.-F.; Chen, P.; Wen, T.-C. $CH_3NH_3PbI_3$ Perovskite/Fullerene Planar-Heterojunction Hybrid Solar Cells. *Adv. Mater.* **2013**, *25*, 3727−3732.

(6) Lee, M. M.; Teuscher, J.; Miyasaka, T.; Murakami, T. N.; Snaith, H. J. Efficient Hybrid Solar Cells Based on Meso-Superstructured Organometal Halide Perovskites. *Science* **2012**, *338*, 643−647.

(7) Stranks, S. D.; Eperon, G. E.; Grancini, G.; Menelaou, C.; Alcocer, M. J. P.; Leijtens, T.; Herz, L. M.; Petrozza, A.; Snaith, H. J. Electron-Hole Diffusion Lengths Exceeding 1 Micrometer in an Organometal Trihalide Perovskite Absorber. *Science* **2013**, *342*, 341−344.

(8) Xing, G.; Mathews, N.; Sun, S.; Lim, S. S.; Lam, Y. M.; Grätzel, M.; Mhaisalkar, S.; Sum, T. C. Long-Range Balanced Electron- and Hole-Transport Lengths in Organic-Inorganic $CH_3NH_3PbI_3$. *Science* **2013**, *342*, 344−347.

(9) Dong, Q.; Fang, Y.; Shao, Y.; Mulligan, P.; Qiu, J.; Cao, L.; Huang, J. Electron-Hole Diffusion Lengths > 175 μm in Solution-Grown $CH_3NH_3PbI_3$ Single Crystals. *Science* **2015**, *347*, 967−970.

(10) Stoumpos, C. C.; Malliakas, C. D.; Kanatzidis, M. G. Semiconducting Tin and Lead Iodide Perovskites with Organic Cations: Phase Transitions, High Mobilities, and Near-Infrared Photoluminescent Properties. *Inorg. Chem.* **2013**, *52*, 9019−9038.

(11) Fang, Y.; Huang, J. Resolving Weak Light of Sub-Picowatt Per Square Centimeter by Hybrid Perovskite Photodetectors Enabled by Noise Reduction. *Adv. Mater.* **2015**, *27*, 2804−2810.

(12) Saidaminov, M. I.; Haque, M. A.; Savoie, M.; Abdelhady, A. L.; Cho, N.; Dursun, I.; Buttner, U.; Alarousu, E.; Wu, T.; Bakr, O. M. Perovskite Photodetectors Operating in Both Narrowband and Broadband Regimes. *Adv. Mater.* **2016**, *28*, 8144−8149.

(13) Saidaminov, M. I.; Adinolfi, V.; Comin, R.; Abdelhady, A. L.; Peng, W.; Dursun, I.; Yuan, M.; Hoogland, S.; Sargent, E. H.; Bakr, O. M. Planar-Integrated Single-Crystalline Perovskite Photodetectors. *Nat. Commun.* **2015**, *6*, 8724.

(14) Zhang, F.; Niu, S.; Guo, W.; Zhu, G.; Liu, Y.; Zhang, X.; Wang, Z. L. Piezo-Phototronic Effect Enhanced Visible/UV Photodetector of a Carbon-Fiber/ZnO-CdS Double-Shell Microwire. *ACS Nano* **2013**, *7*, 4537−4544.

(15) Wang, Z.; Yu, R.; Wen, X.; Liu, Y.; Pan, C.; Wu, W.; Wang, Z. L. Optimizing Performance of Silicon-Based p-n Junction Photodetectors by the Piezo-Phototronic Effect. *ACS Nano* **2014**, *8*, 12866−12873.

(16) Dai, Y.; Wang, X.; Peng, W.; Zou, H.; Yu, R.; Ding, Y.; Wu, C.; Wang, Z. L. Largely Improved Near-Infrared Silicon-Photosensing by the Piezo-Phototronic Effect. *ACS Nano* **2017**, *11*, 7118−7125.

(17) Zhu, L.; Wang, L.; Xue, F.; Chen, L.; Fu, J.; Feng, X.; Li, T.; Wang, Z. L. Piezo-Phototronic Effect Enhanced Flexible Solar Cells Based on n-ZnO/p-SnS Core-Shell Nanowire Array. *Adv. Sci.* **2017**, *4*, 1600185.

(18) Zhu, L.; Wang, L.; Pan, C.; Chen, L.; Xue, F.; Chen, B.; Yang, L.; Su, L.; Wang, Z. L. Enhancing the Efficiency of Silicon-Based Solar Cells by the Piezo-Phototronic Effect. *ACS Nano* **2017**, *11*, 1894−1900.

(19) Chen, M.; Pan, C.; Zhang, T.; Li, X.; Liang, R.; Wang, Z. L. Tuning Light Emission of a Pressure Sensitive Silicon/ZnO Nanowires Heterostructure Matrix through Piezo-Phototronic Effect. *ACS Nano* **2016**, *10*, 6074−6079.

(20) Li, X.; Chen, M.; Yu, R.; Zhang, T.; Song, D.; Liang, R.; Zhang, Q.; Cheng, S.; Dong, L.; Pan, A.; Wang, Z. L.; Zhu, J.; Pan, C. Enhancing Light Emission of ZnO-Nanofilm/Si-Micropillar Heterostructure Arrays by Piezo-Phototronic Effect. *Adv. Mater.* **2015**, *27*, 4447−4453.

(21) Wang, Z. L.; Wu, W. Piezotronics and Piezo-Phototronics: Fundamentals and Applications. *Natl. Sci. Rev.* **2014**, *1*, 62−90.

(22) Wang, Z. L. Progress in Piezotronics and Piezo-Phototronics. *Adv. Mater.* **2012**, *24*, 4632−4646.

(23) Wang, Z. L. The New Field of Nanopiezotronics. *Mater. Today* **2007**, *10*, 20−28.

(24) Kim, Y.-J.; Dang, T.-V.; Choi, H.-J.; Park, B.-J.; Eom, J.-H.; Song, H.-A.; Seol, D.; Kim, Y.; Shin, S.-H.; Nah, J.; Yoon, S.-G. Piezoelectric Properties of $CH_3NH_3PbI_3$ Perovskite Thin Films and Their Applications in Piezoelectric Generators. *J. Mater. Chem. A* **2016**, *4*, 756−763.

(25) Ding, R.; Liu, H.; Zhang, X.; Xiao, J.; Kishor, R.; Sun, H.; Zhu, B.; Chen, G.; Gao, F.; Feng, X.; Chen, J.; Chen, X.; Sun, X.; Zheng, Y. Flexible Piezoelectric Nanocomposite Generators Based on Formamidinium Lead Halide Perovskite Nanoparticles. *Adv. Funct. Mater.* **2016**, *26*, 7708−7716.

(26) Dong, Q.; Song, J.; Fang, Y.; Shao, Y.; Ducharme, S.; Huang, J. Lateral-Structure Single-Crystal Hybrid Perovskite Solar Cells *via* Piezoelectric Poling. *Adv. Mater.* **2016**, *28*, 2816−2821.

(27) Coll, M.; Gomez, A.; Mas-Marza, E.; Almora, O.; Garcia-Belmonte, G.; Campoy-Quiles, M.; Bisquert, J. Polarization Switching and Light-Enhanced Piezoelectricity in Lead Halide Perovskites. *J. Phys. Chem. Lett.* **2015**, *6*, 1408−1413.

(28) Song, J.; Xiao, Z.; Chen, B.; Prockish, S.; Chen, X.; Rajapitamahuni, A.; Zhang, L.; Huang, J.; Hong, X. Enhanced Piezoelectric Response in Hybrid Lead Halide Perovskite Thin Films *via* Interfacing with Ferroelectric $PbZr_{0.2}Ti_{0.8}O_3$. *ACS Appl. Mater. Interfaces* **2018**, *10*, 19218−19225.

(29) Liu, Y.; Yang, Z.; Liu, S. Recent Progress in Single-Crystalline Perovskite Research Including Crystal Preparation, Property Evaluation, and Applications. *Adv. Sci.* **2018**, *5*, 1700471.

(30) Saidaminov, M. I.; Abdelhady, A. L.; Murali, B.; Alarousu, E.; Burlakov, V. M.; Peng, W.; Dursun, I.; Wang, L.; He, Y.; Maculan, G.; Goriely, A.; Wu, T.; Mohammed, O. F.; Bakr, O. M. High-Quality Bulk Hybrid Perovskite Single Crystals within Minutes by Inverse Temperature Crystallization. *Nat. Commun.* **2015**, *6*, 7586.

(31) Chen, Z.; Dong, Q.; Liu, Y.; Bao, C.; Fang, Y.; Lin, Y.; Tang, S.; Wang, Q.; Xiao, X.; Bai, Y.; Deng, Y.; Huang, J. Thin Single Crystal Perovskite Solar Cells to Harvest Below-Bandgap Light Absorption. *Nat. Commun.* **2017**, *8*, 1890.

(32) Liu, Y.; Yang, Z.; Cui, D.; Ren, X.; Sun, J.; Liu, X.; Zhang, J.; Wei, Q.; Fan, H.; Yu, F.; Zhang, X.; Zhao, C.; Liu, S. Two-Inch-Sized Perovskite $CH_3NH_3PbX_3$ (X = Cl, Br, I) Crystals: Growth and Characterization. *Adv. Mater.* **2015**, *27*, 5176−5183.

(33) Leppert, L.; Reyes-Lillo, S. E.; Neaton, J. B. Electric Field- and Strain-Induced Rashba Effect in Hybrid Halide Perovskites. *J. Phys. Chem. Lett.* **2016**, *7*, 3683−3689.

DOI: 10.1021/acsnano.8b06243
ACS Nano XXXX, XXX, XXX−XXX

(34) Poglitsch, A.; Weber, D. Dynamic Disorder in Methylammoniumtrihalogenoplumbates (II) Observed by Millimeter-Wave Spectroscopy. *J. Chem. Phys.* **1987**, *87*, 6373−6378.
(35) Rakita, Y.; Bar-Elli, O.; Meirzadeh, E.; Kaslasi, H.; Peleg, Y.; Hodes, G.; Lubomirsky, I.; Oron, D.; Ehre, D.; Cahen, D. Tetragonal $CH_3NH_3PbI_3$ is Ferroelectric. *Proc. Natl. Acad. Sci. U. S. A.* **2017**, *114*, E5504−E5512.

DOI: 10.1021/acsnano.8b06243
ACS Nano XXXX, XXX, XXX−XXX